

See discussions, stats, and author profiles for this publication at: <https://www.researchgate.net/publication/224003842>

One-Step Synthesis and Self-Assembly of Metal Oxide Nanoparticles into 3D Superlattices

ARTICLE *in* ACS NANO · APRIL 2012

Impact Factor: 12.88 · DOI: 10.1021/nn3010735 · Source: PubMed

CITATIONS

22

READS

57

9 AUTHORS, INCLUDING:



Marc Georg Willinger

Fritz Haber Institute of the Max Planck Society

144 PUBLICATIONS 1,850 CITATIONS

[SEE PROFILE](#)



Feng Liu

University of Queensland

52 PUBLICATIONS 442 CITATIONS

[SEE PROFILE](#)



Xue Bai

Jilin University

4 PUBLICATIONS 50 CITATIONS

[SEE PROFILE](#)



Nicola Pinna

Humboldt-Universität zu Berlin

197 PUBLICATIONS 6,192 CITATIONS

[SEE PROFILE](#)

One-Step Synthesis and Self-Assembly of Metal Oxide Nanoparticles into 3D Superlattices

Andrea Pucci,[†] Marc-Georg Willinger,^{†,‡} Feng Liu,[§] Xiangbing Zeng,[§] Valentina Rebuttini,[†] Guylhaine Clavel,[†] Xue Bai,[†] Goran Ungar,^{§,¶} and Nicola Pinna^{†,‡,*}

[†]Department of Chemistry, CICECO, University of Aveiro, 3810-193 Aveiro, Portugal, [‡]Department of Inorganic Chemistry, Fritz Haber Institute of the Max Planck Society, Berlin, Germany, [§]Department of Materials Science and Engineering, University of Sheffield, Mappin Street, Sheffield S1 3JD, United Kingdom, and [¶]World Class University (WCU) program of Chemical Convergence for Energy & Environment (C2E2), School of Chemical and Biological Engineering, College of Engineering, Seoul National University (SNU), Seoul 151-744, Korea

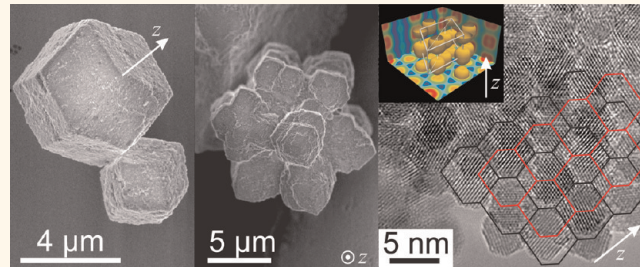
For material scientists, biomineralization offers a playground not only to discover and wonder about beautifully assembled materials, but also to try to mimic them and learn the principles of their formation. During millions of years of evolutionary development and testing, biominerals have evolved in optimized forms under various constraints. A unifying building principle in biominerals is the hierarchical assembly of their building blocks, starting from the basic structural units.^{1–3}

Understanding the formation of materials from their building blocks is essential for the design of hierarchically structured materials. Much work has been devoted to the fabrication of nanoparticles with desired properties; however, their assembly into larger structures is still not fully understood, nor controlled at the molecular level.

Superstructures showing ordered arrangement of nano- or micro-building blocks can be built either by self-assembly directly in solution, or on a substrate following solvent evaporation or sedimentation.^{4–6} Colloidal self-assembly, in particular, has attracted special attention because it allows easy generation of 3D ordered structures.^{7,8} Nano-building blocks can spontaneously organize under the effect of externally applied magnetic, electric, or flow fields, or by specific interaction such as short-range forces.⁹ The large majority of reported approaches fall into the latter category, mainly using substrates, templates, and long aliphatic chain ligands as assembly directing agents.

DNA^{10–14} and liquid crystals^{15,16} driven self-assembly of metal nanoparticles has been one of the most widely investigated methods allowing the engineering of a large number of superlattices. All these

ABSTRACT



A simple one-pot approach based on the “benzyl alcohol route” is introduced for the fabrication of highly ordered supercrystals composed of highly uniform 3–4 nm zirconia and rare-earth stabilized zirconia nanoparticles. The as-fabricated supercrystals reach sizes larger than 10 μm and present well-defined 3D morphologies such as flower-like, rhombic dodecahedron, and bipyramids. This system is unique in that the supercrystals are formed in one-step directly in the reaction medium where the nanoparticles are synthesized. The uniformity in nanocrystal shape and size is attributed to the *in situ* formation of benzoate species that directs the nanoparticle growth and assembly. The low colloidal stabilization of the benzoate-capped nanoparticles in benzyl alcohol promotes the formation of supercrystals in solution by $\pi-\pi$ interaction between the *in situ* formed benzoate ligands attached to neighboring particles. By varying the reaction temperature and the nature of the doping the way the nanobulding blocks assemble in the supercrystals could be controlled. Standard FCC superlattice packings were found together with more unusual ones with $P6/mmm$ and $R\bar{3}m$ symmetries.

KEYWORDS: zirconium oxide · nanoparticles · supercrystals · mesocrystals · assembly · electron microscopy

approaches rely on the use of large and complex ligand molecules. As a consequence, the fraction of organic species in the final material is significant, especially when dealing with small colloids.

Assemblies of nanocrystals stabilized by shorter molecules were also explored.¹⁷ For example, Kahn *et al.* proposed the formation of 2D and 3D arrays of ZnO

* Address correspondence to
pinna@ua.pt,
pinna@snu.ac.kr.

Received for review March 12, 2012
and accepted April 12, 2012.

Published online April 12, 2012
10.1021/nn3010735

© 2012 American Chemical Society

nano particles stabilized by diverse alkyl chains through evaporation of colloidal THF solutions.¹⁸ Better control over dimensionality of the superstructure was achieved by selectively functionalizing either some or all of the faces of silver cubes with a hydrophobic thiolate.¹⁹ Complex 3D structures were also obtained by slow precipitation of CdSe/CdS octapod nanocrystals stabilized with phosphonic-based surfactants.⁵ An interesting example of supercrystal formation is the synthesis of CuS nanocrystals stabilized by dodecanthiol.^{20,21} However, in many cases the production of superstructured materials is a mere laboratory exercise, and robust approaches scalable up to industrial level aimed at commercial applications are still at a research stage.

Surfactant-free nonaqueous (and/or nonhydrolytic) sol–gel routes constitute one of the most versatile and powerful methodologies for the synthesis of nanocrystalline metal oxides with high compositional homogeneity and purity.²² However, one of the drawbacks of these synthesis protocols is the lack of precise control over particle size and size distribution, which is attributable to the lack of stabilizing agents (e.g., surfactants) added to the synthesis. One notable exception is the solvothermal reaction of zirconium isopropoxide in benzyl alcohol leading to the formation of uniform zirconia nanocrystals, which can also be doped by the addition of various metal complexes to the reaction mixture.^{23–26} As will be discussed below, the low size dispersion of the zirconia nanoparticles is tentatively attributed to the *in situ* formation of organic ligands, which make this approach not entirely surfactant-free.

In the present work, the ZrO₂ synthesis is modified by increasing the reaction temperature above 230 °C and by using Tb and Y as dopants. This simple synthetic protocol leads to the formation of benzoate-capped zirconia nanocrystals of uniform shape, size, and orientation that self-assemble into large supercrystals. The present study will show that the main weakness of the surfactant-free nonaqueous routes can be overcome by the *in situ* formation of benzoate species acting as stabilizing and structure-directing agents. The morphology and structure of the supercrystal is studied as a function of the amount of the benzoate species and as a function of nanoparticle doping. To the best of our knowledge, there have been no previous reports of surfactant-free syntheses of nanocrystals coupled with *in situ* assembly into a 3D supercrystal.

RESULTS AND DISCUSSION

Structural Characterization of Zirconia Nanoparticles. Since in this work we use X-ray diffraction to probe both the atomic arrangement in the nanocrystals and the arrangement of nanocrystals in supercrystals, we shall refer to the former as wide-angle XRD (WAXD) and to the latter as small-angle XRD (SAXD). WAXD patterns of

TABLE 1. Composition, Carbon Content, Reaction Temperature, Nanoparticle Size Extracted from Wide-Angle XRD and Packing Arrangement As Determined by SAXD of the Sample Discussed in This Study

composition	carbon content (wt %) ^a	reaction temperature (°C)	particle size (nm) ^b		particle distance (nm)	
			particle packing	between columns	within column	
ZrO ₂	4.4	230	3.7	P6/mmm	4.48	4.87
ZrO ₂	10.5	325	4.4	Fm $\bar{3}m$	6.36	6.36
ZrO ₂	350		4.4	R $\bar{3}m$	6.92	5.71
ZrO ₂ :Tb	14.8	300	3.0	P6/mmm	4.01	4.09
ZrO ₂ :Tb	15.0	325	3.1	R $\bar{3}m$	4.24	3.80
ZrO ₂ :Y	11.1	350	4.3	R $\bar{3}m$	5.91	4.89

^a Deduced from CHN analysis. ^b Crystallite size estimated from WAXD patterns using the Scherrer equation and considering the diffraction peak at $2\theta = 50^\circ$ (*i.e.*, 220); the values are in good agreement with the particle sizes extracted from TEM measurements, suggesting the single crystal nature of the nanoparticles (*cf.* also HRTEM measurements).

the as-synthesized pure zirconia particles are displayed in Supporting Information, Figure S1. They show broad diffraction peaks due to the nanometric size of the crystals. An average particle size around 4 nm, as deduced by the Scherrer formula, is obtained for the pure zirconia particles independently of the reaction temperature (*cf.* Table 1). Due to the broadening of the diffraction peaks it is difficult to assign univocally the crystalline structure of 3–4 nm sized zirconia particles from WAXD experiments.^{23,27} Indeed, the expected WAXD pattern of the cubic (Fm $\bar{3}m$) and tetragonal phase (P4₂/nmc) of zirconia are very similar in this particle size range.²⁷ However, in a previous study, on the basis of Rietveld refinement, it was possible to conclude that the “benzyl alcohol route” leads to the cubic phase for pure zirconia.²³ The yttrium-doped samples consist of particles of similar size, whereas the terbium-doped nanoparticles are slightly smaller (*cf.* Table 1 and Supporting Information, Figure S1). In those specimens the WAXD reflection due to the {111}_{cub}ⁿ lattice planes are broadened and contain a shoulder indicating a deviation from the cubic structure. (Since there are two different scales and structures, (*i.e.*, the atomic arrangement in the nanocrystals and the arrangement of nanocrystals in supercrystals) in order to avoid confusion, a sub and superscript notation of the Miller indices is applied. The superscript “n” and “s” refer, respectively, to nanocrystal and supercrystal, while the subscript denotes the lattice system.) Raman spectra (*cf.* Supporting Information, Figure S2 and discussion) support the stabilization of the tetragonal phase by rare earth ions, similar to what is observed for the bulk.²⁸ The presence of additional crystalline phases is excluded on grounds of there being no WAXD peaks additional to those already discussed, and because all Raman shifts are attributable to a single zirconia phase. Because the difficulty in discriminating between the

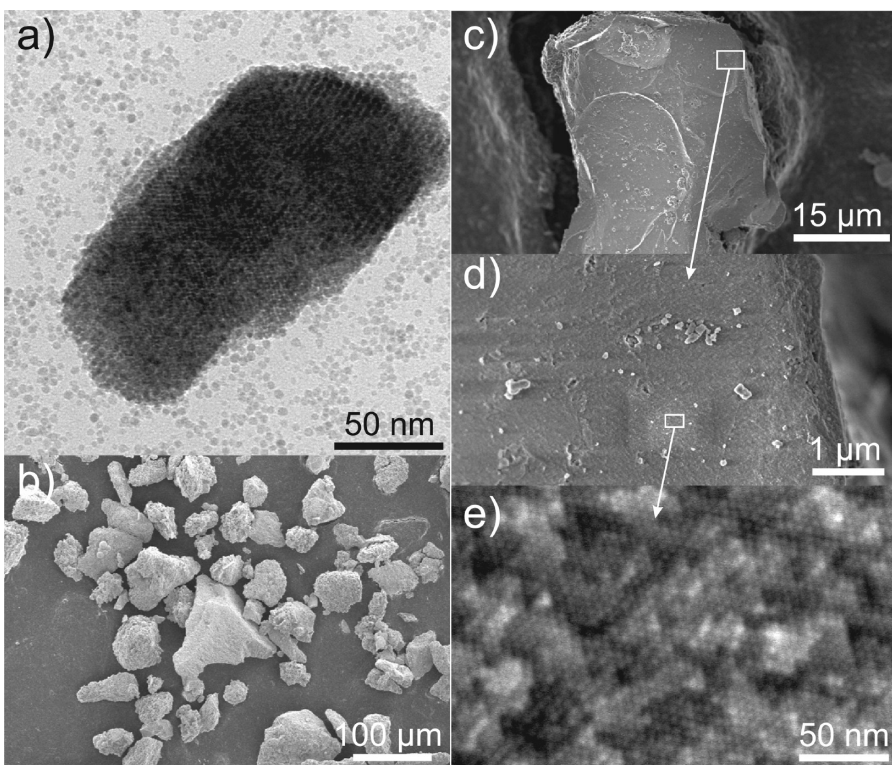


Figure 1. (a) TEM image of a small supercrystals made of ZrO_2 nanoparticles synthesized at $230\text{ }^\circ\text{C}$; (b–e) SEM images recorded at different magnifications on large supercrystals made of ZrO_2 nanoparticles synthesized at $325\text{ }^\circ\text{C}$.

cubic and tetragonal zirconia modifications in the 3–4 nm size range by WAXD, and therefore also by high resolution transmission electron microscopy and selected area electron diffraction, hitherto we will only use the cubic ($Fm\bar{3}m$) modification to denote lattice planes and directions.

Nanoparticle Assembly. Transmission electron microscopy (TEM) studies of the standard sample synthesized at $230\text{ }^\circ\text{C}$ principally show isolated nanoparticles, but also some supercrystals such as the one in Figure 1a. They are composed of monodisperse particles of about 4 nm, that is, the same size as isolated nanoparticles but assembled periodically. This first observation motivated us to investigate the factors controlling the assembly behavior of zirconia nanoparticles. An increase in reaction temperature did not dramatically affect either the zirconia particle size or their size distribution. On the other hand, large aggregates of several tens of micrometers were now present as shown by the scanning electron microscopy (SEM) images (Figure 1b,c). Zooming in on one of these aggregates reveals that they are composed of 4 nm zirconia nanoparticles assembled in ordered structures (Figure 1d,e). Therefore, a simple increase in reaction temperature has the effect of promoting nanoparticle assembly into large supercrystals without affecting the nanocrystal size.

It was shown recently that zirconia nanoparticles synthesized in benzyl alcohol could be homogeneously doped with various transition metals and euro-

pium.^{24–26} The fabrication of terbium-doped zirconia should take place at higher temperatures compared to pure zirconia. As a matter of fact, at temperatures lower than $300\text{ }^\circ\text{C}$ the yield of the reaction was lower than 30%. At $300\text{ }^\circ\text{C}$ nanoparticles forming large ill-defined objects could be obtained (Figure 2a). It turned out that they are composed of monodisperse terbium-doped zirconia nanoparticles assembled in well-ordered superlattices. Figure 2b shows the edge of a supercrystal containing several layers of hexagonally assembled nanoparticles. The Fourier transform (FT) of the whole image shows two sets of reflections, the outer ones attributed to the ZrO_2 structure and the inner ones, attributed to the packing of nanoparticles (Figure 2c). It illustrates very graphically the orientational correlation between the nanocrystal and supercrystal lattices. The two outer sets of reflections can be attributed to the cubic zirconia structure in $[110]_{\text{cub}}^n$ zone axis. The outer spots ($\{111\}_{\text{cub}}^n$ and $\{220\}_{\text{cub}}^n$) are arranged with hexagonal symmetry, with a degree of azimuthal spread. This is understandable since the $\bar{3}$ axis of the cubic ZrO_2 , that is, $[111]_{\text{cub}}^n$, is not parallel to the overall hexagonal symmetry axis of the FT image; instead it is the $[110]_{\text{cub}}^n$, that is parallel to it, inevitably leading to arcing of the outer FT spots. The presence of six reflections due to the $\{220\}_{\text{cub}}^n$ lattice planes suggests that the nanocrystals can rotate in steps of $\sim 60^\circ$ around the $[110]_{\text{cub}}^n$ axis. The $[110]_{\text{cub}}^n$ orientation is further supported by the FT calculated on single particles such as the one shown

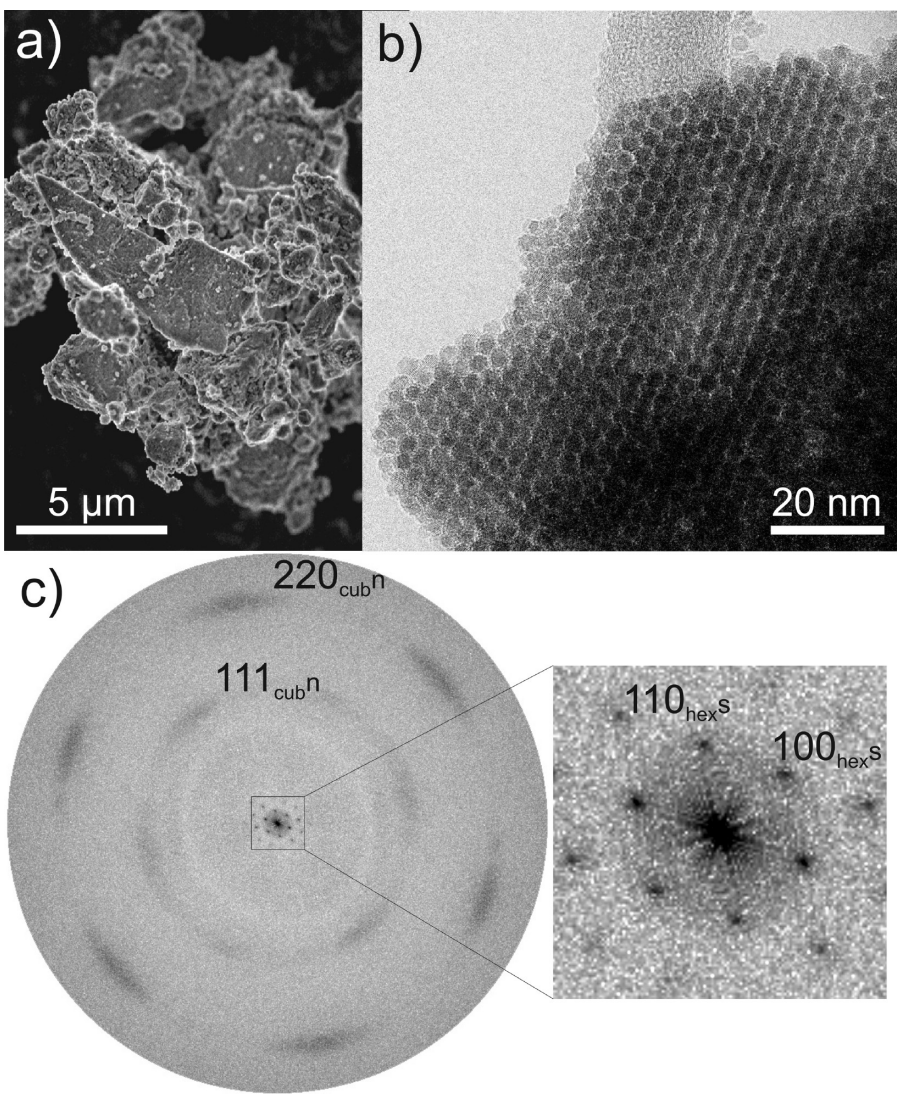


Figure 2. (a) SEM and (b) TEM images of supercrystals of 10% Tb-doped zirconia synthesized at 300 °C. (c) FT of the whole image in panel b and a magnified part of center.

in Supporting Information, Figure S3. Close to the center, two families of reflections can be distinguished (this part, almost indiscernible, is indicated by a square and is magnified in the right part of Figure 2c), they are characteristic of a 2D hexagonal packing of the nanoparticles.

Since transmission and scanning electron microscopy are not the best techniques for the assessment of the nanoparticles 3D-packing and because the synthesis approach readily produces a gram quantity of material, the nanoparticle assembly was studied by small-angle X-ray diffraction (SAXD). The unusual packing of the nanoparticles is manifested in the relatively sharp SAXD peaks (*cf.* the figures and detailed explanation for each sample in the Supporting Information). Figure 3 shows a typical SAXD pattern recorded from a FCC assembly together with the best fit-curve and the resolved diffraction peaks. The packing of the zirconia nanoparticles strongly depends on

temperature. For the lower temperatures of synthesis (*i.e.*, 230 °C for pure zirconia and 300 °C for 10% Tb-doped zirconia) a 3D simple hexagonal lattice with space group *P*6/*mmm* is found. The reconstructed electron density map (Figure 4a) shows that the nanoparticles are centered at the corners of the hexagonal unit cell. The cell parameters are $a = 4.01$ nm (the distance between nanoparticles within the {001} hexagonal plane) and $c = 4.09$ nm (distance between particles within a column, normal to the hexagonal plane) for the 10% Tb-doped zirconia synthesized at 300 °C. The isoelectron surface enclosing the high density region (*i.e.*, the core of the nanoparticles) shows disproportionately large elongation along the *c*-axis, suggesting relatively poor correlation along the column. By comparing the TEM (Figure 2b,c) and the SAXD data, it is clear that the $[001]_{\text{hex}}^{\text{s}}$ of the *P*6/*mmm* superlattice is normal to the plane of the image in Figure 2b, that is, parallel to the $[110]_{\text{cub}}^n$.

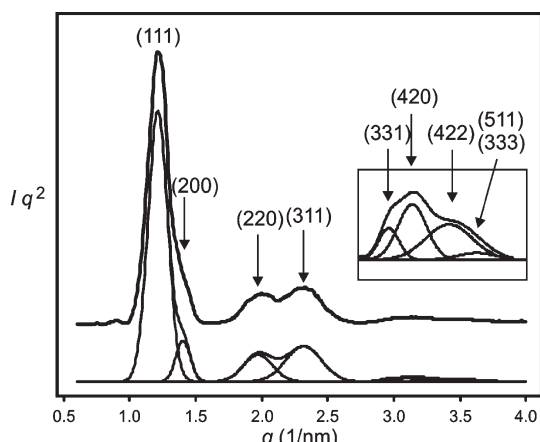


Figure 3. SAXD of ZrO_2 synthesized at $325\text{ }^\circ\text{C}$, FCC ($Fm\bar{3}m$) phase. Best fit-curve and resolved diffraction peaks are plotted below for comparison. The last four peaks are expanded vertically 15 times and shown in the inset.

At higher reaction temperatures (*i.e.*, 325 and $350\text{ }^\circ\text{C}$) the synthesis produces supercrystals with well-faceted shapes such as flower-like, rhombic dodecahedron, and bipyramids, depending on the temperature and dopant used. At $325\text{ }^\circ\text{C}$ the terbium-doped particles mainly show a flower-like morphology (Figure 5a). SEM images of isolated supercrystals highlight the complex morphology and growth pattern (Figure 5b,c). The overview TEM image (Figure 5d) shows the facets and the complexity of the leaves. The three pairs of reflections present in the selected area electron diffraction are characteristic of the cubic zirconia in the [110] orientation (Figure 5e). Here again the nanocrystals exhibit a preferential crystallographic orientation. The higher resolution image of the same edge of the aggregate, from which the SAED was recorded, shows the nanobuilding blocks forming an ordered superlattice (Figure 5f). Increasing the reaction temperature to $350\text{ }^\circ\text{C}$ results in rhombic dodecahedron supercrystals, in addition to flower-like morphologies, such as the ones shown in Figure 5g. The yttrium-doped sample synthesized under the same conditions shows bipyramid supercrystals (Figure 5h). The HRSEM images of the surface of the well-faceted supercrystals always show a highly ordered assembly of the nanobuilding blocks (*cf.* Figure 5i).

It is important to point out that irrespective of the synthesis temperature and the doping the resulting nanoparticles have similar size (*i.e.*, between 3.0 and 4.4 nm, *cf.* Table 1). Combined with the fact that the nanobuilding blocks are not completely fused and are therefore still discernible, these unique features allow us to study the formation mechanism of the supercrystals.

By increasing the reaction temperature the packing changes as well; for the pure samples it passes from the 3D simple hexagonal lattice with space group $P6/mmm$ via a face centered cubic lattice (FCC) with space group

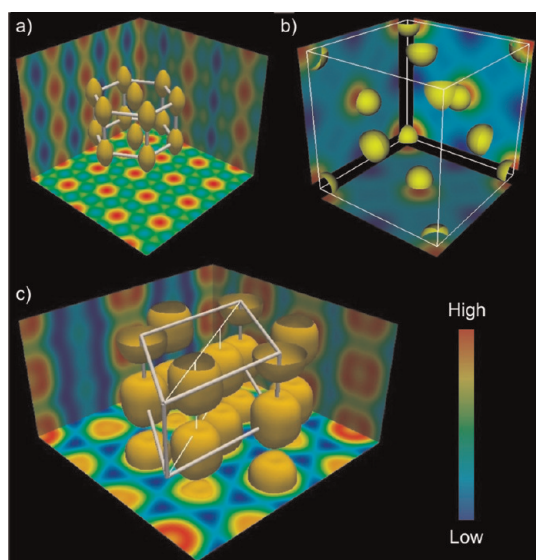


Figure 4. Reconstructed electron density maps of the superlattices: (a) ZrO_2 synthesized at $230\text{ }^\circ\text{C}$; $P6/mmm$ lattice. Isoelectron surfaces enclose the regions of highest average electron density, that is, the central portions of the nanoparticles; (b) ZrO_2 synthesized at $325\text{ }^\circ\text{C}$; $Fm\bar{3}m$ (FCC) lattice; (c) 10% Tb-doped ZrO_2 synthesized at $325\text{ }^\circ\text{C}$; $R\bar{3}m$ lattice. In panels a and c the three orthogonal 2D maps lining the walls are [100], [110] and [001] cuts, referring to hexagonal coordinates.

symmetry $Fm\bar{3}m$, to a rhombohedral lattice with space group $R\bar{3}m$. The reconstructed electron density map of the FCC phase (Figure 4b) shows the well-known close-packed structure of hard spheres, with each nanoparticle surrounded by 12 nearest neighbors, 6.36 nm apart from each other. Because of the higher correlation length, the $R\bar{3}m$ packing is more easily studied on doped samples, and this structure will thus be discussed further below.

Similar packings, with symmetries $P6/mmm$ (synthesized at $300\text{ }^\circ\text{C}$) and $R\bar{3}m$ (325 and $350\text{ }^\circ\text{C}$), are observed for doped nanoparticles (Table 1). According to the SAXD diffraction pattern, the $R\bar{3}m$ superlattice of Tb-doped ZrO_2 nanoparticles synthesized at $325\text{ }^\circ\text{C}$ has lattice parameters $a = 7.01\text{ nm}$ and $c = 3.80\text{ nm}$ (hexagonal coordinates). The reconstructed electron density map (Figure 4c) shows that ZrO_2 nanoparticles form linear chains. The distance between nanoparticles in each chain is $c = 3.80\text{ nm}$. The nanoparticle columns pack on a hexagonal lattice, with the columns shifted longitudinally by $c/3 = 1.27\text{ nm}$ relative to the neighboring columns. Consequently, each unit cell contains 3 chains of nanocrystals with a relative longitudinal shift of 0, 1.27, and 2.53 nm, respectively. In contrast to the simple hexagonal packing of low-temperature synthesized nanoparticles, here the nearest distance between nanoparticles in neighboring chains is larger (4.24 nm) than within the same chain (3.80 nm) (see Table 1). This rhombohedral structure can in fact be viewed either as a BCC or a FCC structure compressed along the [111] axis. In terms of packing of nearest

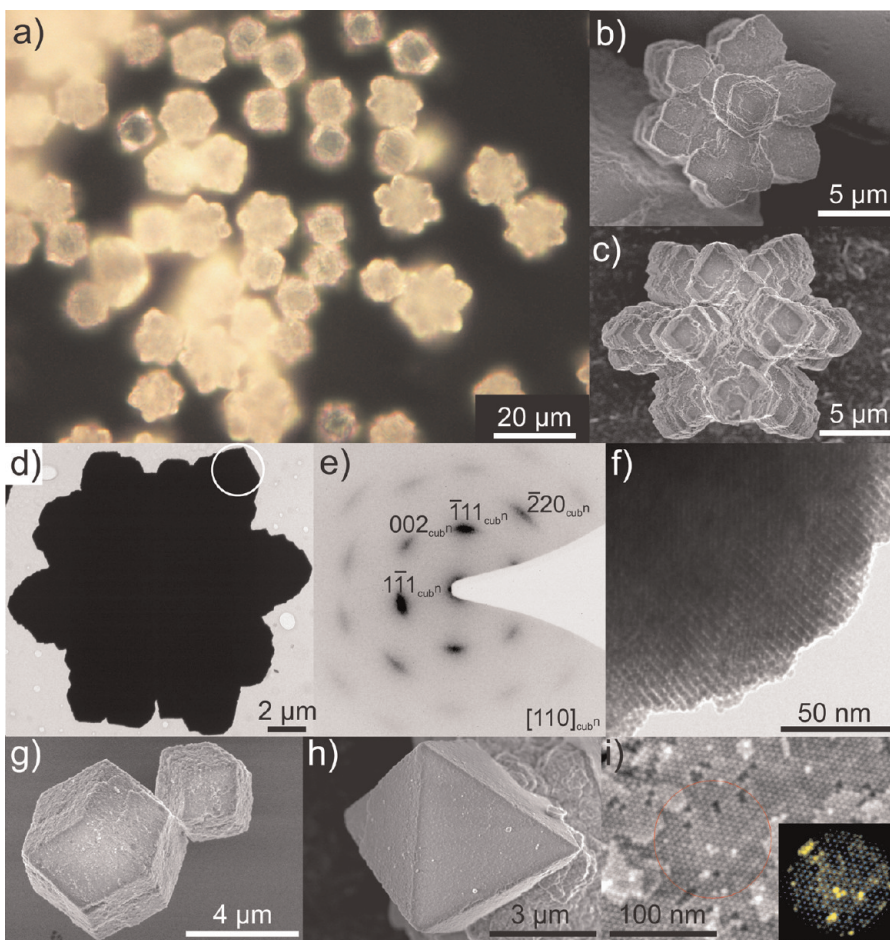


Figure 5. (a) Optical micrograph, (b,c) SEM, and (d,f) TEM images of supercrystals of 10% Tb-doped zirconia synthesized at 325 °C; (e) selected area electron diffraction of the region indicated by a circle in panel d; (g) SEM of rhombic dodecahedra supercrystals of 10% Tb-doped zirconia synthesized at 350 °C; (h) SEM of bipyramidal supercrystal of 6% Y-doped zirconia synthesized at 350 °C; (i) HRSEM of the surface of an aggregate showing the assembly of the nanocrystal building blocks (inset: color coded image showing a different layer of nanoparticles).

neighbor particles, this rhombohedral phase is closer to BCC (shrunk by 13% along z) than FCC, both possessing a $\bar{3}$ axis. The order in the rhombohedral phase is quite high, judging by the FWHW of the (110) diffraction peak (*cf.* Supporting Information, Figure S12) which gives a domain size of ~ 63 nm.

High resolution TEM of an edge of a supercrystal gives additional information on nanoparticle packing. In Figure 6a several layers of particles were imaged in high resolution. The slight difference in contrast makes it possible to distinguish the edges and the shape of the individual nanobuilding blocks. The particles are well-faceted showing nonequilateral hexagonal projections. Each nanocrystal shows well-defined lattice fringes. The FT of the lattice fringes of the whole image (Figure 6b) consists of azimuthally spread spots, the distance and the angle between them being characteristic of the cubic ZrO_2 structure imaged along the $[110]_{\text{cub}}^n$ zone axis. One of the particles, delineated by the yellow contour in panel (a), was further magnified in Figure 6d showing the mask used in the Fourier transformation (Figure 6e). The FT spots of this smaller

region exhibit no arcing, in contrast to the FT calculated from the whole assembly (Figure 6b). The spots are again characteristic of the cubic ZrO_2 structure imaged along the $[110]_{\text{cub}}^n$ axis, proving that the azimuthal spread of the spots in Figure 6b is due to slight crystallographic misorientation of the nanobuilding blocks.

The HRTEM picture (Figure 6a) agrees very well with the $R\bar{3}m$ superlattice determined from SAXD, viewed along the $[100]_{\text{rho}}^s = [110]_{\text{cub}}^n$ direction. (In this paper we use hexagonal coordinate axes to describe the rhombohedral lattice, so $[100]_{\text{rho}}^s$ is orthogonal to $[001]_{\text{rho}}^s$ or the z -axis.) If we replace each nanoparticle with its Voronoi cell, as outlined in black and red in Figure 6a, it becomes clear that the outlines correspond well with the identifiable edges of the nanoparticles. In Figure 6a one can clearly see the columns formed by the stacking of nanoparticles along z (rhombohedral $[001]_{\text{rho}}^s$). The shift along z between neighboring columns can also be clearly seen. The Voronoi cell of the $R\bar{3}m$ phase is found to be very close to a regular cuboctahedron of a BCC structure. The two Voronoi cells are compared in

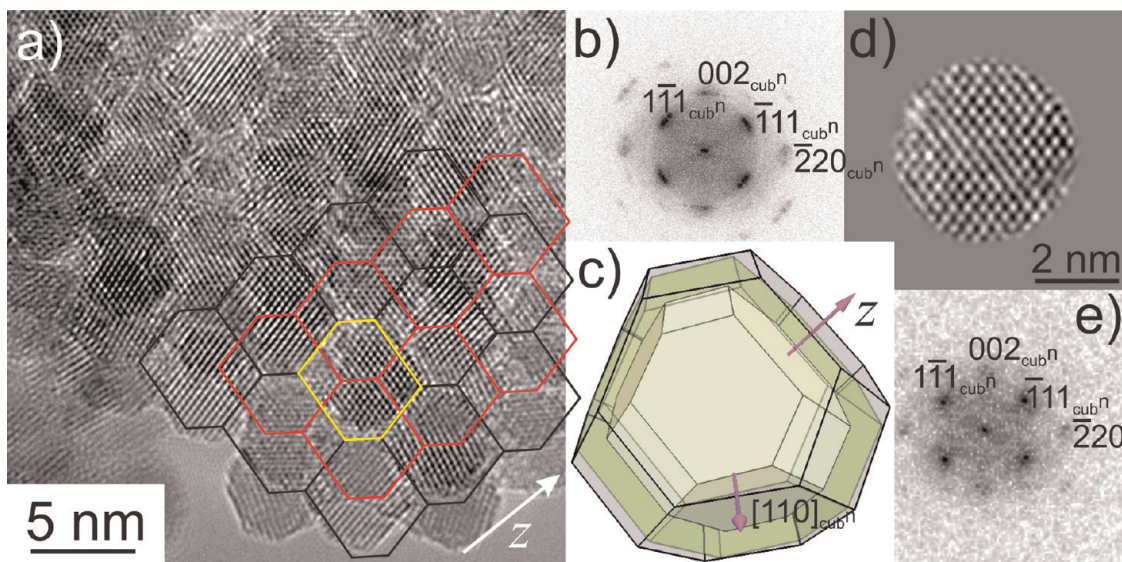


Figure 6. (a) HRTEM image of a superlattice made of 6% Y-doped ZrO_2 synthesized at $350\text{ }^\circ\text{C}$. The black and red lines represent two layers of the Voronoi cells drawn around the ideal center $(0,0,0)$ position of each nanoparticle in the $\text{R}\bar{3}m$ superlattice, projected along $[110]_{\text{cub}}^n$ axis of the nanoparticles. These projected polyhedra closely match the observed outlines of the particles in the TEM image. (b) FT of the region of the supercrystal shown in panel a. (c) Three Voronoi polyhedra drawn around the $0,0,0$ positions, i.e., the ideal center of the nanoparticle; the outer one (gray) is the perfect cuboctahedron that would tessellate a BCC lattice (point symmetry $m\bar{3}m$); the middle polyhedron (green) tessellates the $\text{R}\bar{3}m$ lattice (point symmetry $3m$) with lattice parameters observed in the case of 6% Y-doped ZrO_2 synthesized at $350\text{ }^\circ\text{C}$. The distortion of the $\text{R}\bar{3}m$ along the z -axis is obvious. The inner Voronoi is that of the lattice shrunk upon annealing at $425\text{ }^\circ\text{C}$ (cf. following section). (d) HRTEM of the selected particle used for the FT shown in panel e; the same particle is highlighted by the yellow contour in panel a.

Figure 6c. The outer two polyhedra are the cuboctahedron of the BCC packing in gray, and the distorted cuboctahedron found in our $\text{R}\bar{3}m$ packing in green. The distortion (*i.e.*, compression) along the $[111]_{\text{cub}}^n$ (*i.e.*, z) axis is obvious for the $\text{R}\bar{3}m$ compared to the cuboctahedron of the BCC structure. There are eight $\{111\}_{\text{cub}}^n$ and six $\{100\}_{\text{cub}}^n$ facets in a cuboctahedron. For $\text{R}\bar{3}m$ the hexagonal symmetry of two of the $\{111\}_{\text{cub}}^n$ facets (normal to z) is preserved, while the other $\{111\}_{\text{cub}}^n$ facets are slightly distorted, and the $\{100\}_{\text{cub}}^n$ facets become rectangular rather than square.

Discussion of the Assembly Mechanism. To better understand the factors controlling the nanoparticle assembly, additional characterization has been carried out. First of all, it is known that supercrystals are generally formed by interactions between the ligands adsorbed at the surface of the nanoparticles. Although no surfactants are used in the present synthesis, a careful investigation of the organic species left at the surface of the zirconia nanoparticles was carried out by ^{13}C solid state NMR and FT-IR spectroscopy (cf. Figures S4 and S5 and the discussion in the Supporting Information). In all the cases, carbon contamination was observed (cf. Table 1). More surprisingly, it was found that the only organic species detected are benzoates. *In situ* formed benzoate species coming from the oxidation of benzyl alcohol used as solvent for the metal oxide synthesis have been observed previously.²⁹ They are usually formed at relatively high temperatures and can be catalyzed by metal centers. A peculiar example is the formation of rare-earth (RE)

oxide-based lamellar organic–inorganic nanostructures under similar reaction conditions.^{29–31} For example, it was found that benzoate species were the only organic moieties present between the inorganic RE_2O_3 layers, separating them by 1.2 nm. They form bridging bidentate coordination to the RE_2O_3 layers, and are responsible for the formation of the periodic organic–inorganic structure *via* π – π stacking. Moreover, the assembly of gold nanorods due to π – π stacking was recently demonstrated upon addition of salicylates (hydroxybenzoates) molecules.³² From chemical analysis the concentration of organic “contamination” increases with the reaction temperature and the doping (cf. Table 1). Indeed, the carbon content estimated from elemental and thermogravimetric analysis was less than 5 wt % for the standard synthesis of ZrO_2 nanoparticles at $230\text{ }^\circ\text{C}$ and it increased up to 15% for the nanoparticles synthesized above $300\text{ }^\circ\text{C}$. From FT-IR spectra a bridging bidentate coordination between benzoate species and zirconium ions is found (cf. Figure S5 and discussion in the Supporting Information). It should also be pointed out that the mother liquor after nanoparticle formation (not shown) does not contain any benzoic acid, while it shows the presence of toluene and benzaldehyde (*i.e.*, the by-products of the disproportion of benzyl alcohol involved in the benzoate formation²⁹). Moreover, had benzoic acid been present in the solution, it would have reacted, under the reaction conditions applied, with the solvent (*i.e.*, benzyl alcohol), leading to the formation of the corresponding ester and water; traces

of benzylbenzoate were actually found in the NMR spectra. A test reaction in the presence of benzoic acid was also carried out, unfortunately its presence changes the reaction conditions promoting a hydrolytic mechanism and the formation of monoclinic zirconia nanoparticles (not shown). These analyses and control experiments prove that benzoate species are formed at the surface of the nanoparticles, staying adsorbed and stopping their further growth. The low polydispersity of the ZrO_2 nanoparticles, compared to similar surfactant-free nonaqueous sol–gel routes, supports this mechanism. These findings suggest that the formation of the zirconia supercrystals could be attributed to the surface benzoate species, where $\pi-\pi$ stacking between phenyl groups keeps the structure together and directs the assembly. Generally, the primary particle sizes extracted from WAXD linewidths and TEM measurements are in good agreement, pointing to a single crystal characteristic of the particles as also previously demonstrated.^{24,26} On the other hand, the particle–particle distance determined from SAXD experiments is always larger than the particle size (cf. Table 1). This implies that organic species acting as glue are intercalated in the superlattice and participate in its assembly.

To confirm the above hypothesis selected samples were subjected to mild heat treatment to remove the organic species while preserving the order. At the same time, the assembly and lattice contraction was monitored by SAXD. Annealing at 400 °C for 1 h led to a weight loss of 18% and a contraction of the lattice parameters larger than 20% for the 10% Tb-doped nanoparticles synthesized at 300 °C. The parameters of the simple hexagonal ($P6/mmm$) lattice contracted slightly nearly isotropically from $a = 4.01$ and $c = 4.09$ nm to $a = 3.49$, $c = 3.58$ nm, that is, by 13.0% and 12.5% along a and c , respectively. It should also be pointed out that the structure of the superlattice was not affected by thermal treatment up to 400 °C (cf. Figure S15 and discussion in the Supporting Information). Similar results were obtained for the 10% Tb-doped nanoparticles synthesized at 325 °C. In the latter case, the $R\bar{3}m$ structure and the order were retained for annealing up to 400 °C, while the lattice parameters decreased anisotropically from $a = 7.01$ nm, $c = 3.80$ nm to $a = 6.30$ nm, $c = 3.17$ nm, that is, by 10.1% and 16.5% along a and c , respectively. Increasing the annealing temperature to 425 °C led to a further steep contraction of the lattice to $a = 5.85$ nm and $c = 2.97$ nm, as well as to a rapid deterioration and finally loss of order (cf. Figure S16 and discussion in Supporting Information). The relative shrinkage of the nanocrystals on thermal treatment, particularly in the c direction, is seen more clearly by comparing the green intermediate polyhedron in Figure 6c (average nanoparticle shape before treatment) with the white innermost polyhedron (nanoparticle after heat treatment).

The gap between the surfaces of these two polyhedra had originally been filled by the organic ligand, which disappeared on thermal treatment. These experiments thus prove that the supercrystals are formed due to organic ligands stabilizing the nanocrystals.

After the assessment of the mechanism leading to the ordered assembly of the nanoparticles, the factors governing the assembly toward one structure or another have to be discussed. Both the reaction temperature and doping affect particle size, benzoate formation, and packing. Generally, increasing the temperature leads to larger particles (cf. Table 1). Moreover, the quantity of benzoate species increases with the reaction temperature and with doping. The latter can be attributed to the catalytic effect of the lanthanide ions on the oxidation of benzyl alcohol to benzoate species as already demonstrated in previous reports.^{29,30,33}

The assumption that it is the accumulation of benzoate groups that poison the growth faces and limit particle growth to a uniform size is supported by the fact that a low amount (e.g., below 5 wt %) of benzoate does not allow the formation of large supercrystals, such as for particles synthesized at 230 °C. The next question is what causes nanocrystals of cubic lattice symmetry to form anisotropic particles which, moreover, pack with long-range orientational order. As shown, the anisotropy only develops at higher temperatures of synthesis, where the surface density of benzoate groups is high. Although this is difficult to prove with the techniques at our disposal, we propose that under such circumstances the densely packed benzoate rings exhibit a nematic-like structure, similar to that in nematic discotic liquid crystals. The resulting difference in inclination of benzoate groups on different nanocrystal facets means that the effective poisoning of particle growth is different on different facets. As it happens, it is most effective on $\{001\}_{\text{rho}}^n$ facets, leading to oblate cuboctahedra. We note that there is a precedent in liquid crystal ligands, albeit rod-like rather than disk-like, effecting anisotropic packing of isotropic gold nanoparticles; interestingly, this packing is also on a $R\bar{3}m$ lattice.¹⁶ It has also been shown recently that a dilution of the nematogen ligand leads to a loss of anisotropy and, quite remarkably, also to formation of the FCC structure.³⁴

The remaining question is where the FCC superlattice in ZrO_2 fits in the present scheme. In doped ZrO_2 the transition from $P6/mmm$ to $R\bar{3}m$ is direct, but in pure ZrO_2 it happens via the FCC. Table 1 shows that the interparticle distance in FCC is the average of the distances in $R\bar{3}m$. This suggests that the FCC is in fact made up of small domains of $R\bar{3}m$ that are randomly oriented along all four $[111]_{\text{FCC}}^s$ directions. Thus FCC appears to be the symmetry of long-range order, but locally the symmetry may still be $R\bar{3}m$. Then on further increase in reaction temperature one direction prevails and $R\bar{3}m$ becomes the symmetry of the

long-range order. As mentioned above, our $R\bar{3}m$ phase can be regarded as FCC compressed along [111] and distorted further.

CONCLUSION

Compared to previous reports on self-assembly of nanoparticles, our system is unique in that the supercrystals are self-assembled directly in the reaction medium where the nanoparticles are formed. This is in contrast to the generally used strategy where supercrystals are formed by slow evaporation of the solvent from a stable colloidal suspension of ligand-capped particles. The low colloidal stabilization of the benzoate capped nanoparticles in benzyl alcohol promotes the formation of stable supercrystals in solution by $\pi-\pi$ interaction between the *in situ* formed benzoate ligands attached to neighboring particles. The as-fabricated

supercrystals reach sizes larger than 10 μm and present well-defined 3D morphologies such as flower-like, rhombic dodecahedron, and bipyramids that can be controlled by adjusting the reaction parameters. Indeed, the reaction temperature and doping have an effect on the amount of benzoate species present at the surface of the particles, which causes the nanoparticles to self-assemble in unusual superlattices.

Finally, using this strategy we were able to easily fabricate a gram quantity of highly hierarchically structured supercrystals. The 3–4 nm building blocks could be assembled in superlattices that are normally not achievable for nanoparticles capped with common surfactants. Because of the versatility of the synthetic approach similar assemblies might be obtained with other metal oxides.

METHODS

Chemicals. Zirconium(IV) isopropoxide isopropyl alcohol complex 99.9%, terbium(III) acetate hydrate 99.9%, yttrium(III) isopropoxide oxide and benzyl alcohol 99%, were purchased from Aldrich. All the precursors were stored in a glovebox and used as received.

Synthesis. Nanomaterial syntheses were performed in an argon-filled glovebox (levels of O_2 and H_2O below 1 ppm). In a typical reaction, a glass vessel of 45 mL inner volume was filled with 250 mg (0.645 mmol) of zirconium(IV) isopropoxide isopropyl alcohol complex and 10 mL of benzyl alcohol. In the case of the doped samples, 24 mg (0.071 mmol corresponding to 10% doping) of terbium(III) acetate or 10 mg (0.008 mmol corresponding to 6% doping) of yttrium(III) isopropoxide oxide were added to the reaction mixture. The vessel was slid into a steel autoclave, sealed, removed from the glovebox, and then heated for 2 days in a furnace at the needed temperature (230, 300, 325, and 350 °C). The resulting suspensions were centrifuged and the precipitates were washed with ethanol and acetone and afterward dried in air at 60 °C. The powders are white for both pure and doped oxides.

Characterization Techniques. The wide-angle X-ray powder diffraction (WAXD) data were collected on an X'Pert MPD Philips diffractometer ($\text{Cu K}\alpha$ radiation at 40 kV and 50 mA). Transmission electron microscopy (TEM) was carried out on a Hitachi H-9000 microscope operating at 300 kV. High resolution TEM (HRTEM) was performed using a CM200FEG (Philips) microscope with a field emission gun or a Jeol 2200FS, both microscopes were operated at 200 kV. Samples were prepared by depositing a drop of a suspension of particles in ethanol on a copper grid coated with an amorphous carbon film. Scanning electron microscopy (SEM) investigations were carried using a HR-SEM Hitachi SU-70 and a Hitachi S-4800 operated between 2 and 30 kV acceleration voltage. ^{13}C NMR spectra were recorded at 9.4 T on a Bruker Avance 400WB spectrometer (DSX model) on a 4 mm BL Cross-polarization magic angle spinning (CPMAS) VTN probe at 100.61 MHz. Fourier transform infrared spectroscopy (FT-IR, Spectrum BX, Perkin-Elmer) was carried out in the range of 4000–350 cm^{-1} in transmission mode. The pellets were prepared by adding 1–2 mg of the nanopowder to 100 mg of KBr. The mixture was then carefully mixed and compressed at a pressure of 10 MPa to form transparent pellets. Raman spectroscopy was carried out with a frequency-doubled Nd:YAG laser at a 532 nm excitation wavelength directly on the powder.

The small-angle X-ray diffraction (SAXD) experiments were carried out at station I22, Diamond Light Source and Station BM28, ESRF. The wavelength used was 0.65 Å. 2-Dimensional

SAXD patterns were recorded using a Mar165 CCD detector, and converted to 1-D curves by radial averaging. The measurement of the positions and intensities of the diffraction peaks is carried out using the Galactic PeakSolve program, where experimental diffractograms are fitted using Gaussian shaped peaks. The diffraction peaks are indexed on the basis of their peak positions, and the lattice parameters and the space groups are subsequently determined. Once the diffraction intensities are measured and the corresponding space group determined, 3-D electron density maps can be reconstructed, on the basis of the general formula

$$E(xyz) = \sum_{hkl} F(hkl) \exp[i2\pi(hx + ky + lz)] \quad (1)$$

Here $F(hkl)$ is the structure factor of a diffraction peak with index (hkl) . It is normally a complex number, and the experimentally observed diffraction intensity is

$$I(hkl) = K \cdot F(hkl) \cdot F^*(hkl) = K \cdot |F(hkl)|^2 \quad (2)$$

Here K is a constant related to the sample volume, incident beam intensity, etc. In this paper we are only interested in the relative electron densities, hence this constant is simply taken to be 1. Thus the electron density is

$$E(xyz) = \sum_{hkl} \sqrt{|F(hkl)|} \exp[i2\pi(hx + ky + lz) + \phi_{hkl}] \quad (3)$$

As the observed diffraction intensity $I(hkl)$ is only related to the amplitude of the structure factor $|F(hkl)|$, the information about the phase of $F(hkl)$, ϕ_{hkl} , cannot be determined directly from experiment. However, the problem is greatly simplified when the structure of the ordered phase is centrosymmetric, and hence the structure factor $F(hkl)$ is always real and ϕ_{hkl} is either 0 or π .

This makes it possible for a trial-and-error approach, where candidate electron density maps are reconstructed for all possible phase combinations, and the “correct” phase combination is then selected on the merit of the maps, helped by prior physical and chemical knowledge of the system. This is especially useful for the study of nanostructures, where normally only a limited number of diffraction peaks are observed.

Conflict of Interest: The authors declare no competing financial interest.

Acknowledgment: This work was partially supported by the WCU (World Class University) program through the National Research Foundation (NRF) of Korea funded by the Ministry

of Education, Science and Technology (R31-10013), by FCT projects PTDC/CTM/100468/2008, REDE/1509/RME/2005, SFRH/BPD/71671/2010, SFRH/BD/68810/2010, and SFRH/BD/45177/2008, and by the EU FP7 project NANOGOLD (No. 228455). We are grateful to O. Bikondoa, D. Mannix, S. Brown and P. Thompson at BM28 (XMaS) beamline, ESRF, and to J. Hiller and N. Terrill at I22 at Diamond for help with the SAXD experiments, and to A. J. S. Fernandes from the Physics Department of the University of Aveiro for Raman spectroscopy. Prof. Edson Roberto Leite from Federal University of São Carlos is warmly acknowledged for a discussion at the MRS fall meeting 2011 on the zirconium oxide synthesis following the “benzyl alcohol route” and on his experiments similar to the one reported in this manuscript.

Supporting Information Available: WAXD patterns, Raman spectrum, and data analysis, additional HRTEM images, solid state NMR spectra and data analysis, FT-IR spectra and data analysis, SAXD patterns and data analysis of as-synthesized and heat treated samples. This material is available free of charge via the Internet at <http://pubs.acs.org>.

REFERENCES AND NOTES

- Cölfen, H.; Antonietti, M. Mesocrystals: Inorganic Superstructures Made by Highly Parallel Crystallization and Controlled Alignment. *Angew. Chem., Int. Ed.* **2005**, *44*, 5576–5591.
- Cölfen, H.; Mann, S. Higher-Order Organization by Mesoscale Self-Assembly and Transformation of Hybrid Nanosstructures. *Angew. Chem., Int. Ed.* **2003**, *42*, 2350–2365.
- Song, R.-Q.; Cölfen, H. Mesocrystals-Ordered Nanoparticle Superstructures. *Adv. Mater.* **2009**, *22*, 1301–1330.
- Henzie, J.; Grunwald, M.; Widmer-Cooper, A.; Geissler, P. L.; Yang, P. Self-Assembly of Uniform Polyhedral Silver Nanocrystals into Densest Packings and Exotic Superlattices. *Nat. Mater.* **2012**, *11*, 131–137.
- Miszta, K.; de Graaf, J.; Bertoni, G.; Dorfs, D.; Brescia, R.; Marras, S.; Ceseracciu, L.; Cingolani, R.; van Roij, R.; Dijkstra, M.; et al. Hierarchical Self-Assembly of Suspended Branched Colloidal Nanocrystals into Superlattice Structures. *Nat. Mater.* **2011**, *10*, 872–876.
- Tanaka, A.; Kamikubo, H.; Kataoka, M.; Hasegawa, Y.; Kawai, T. Size-Controlled Aggregation of Cube-Shaped EuS Nanocrystals with Magneto-optic Properties in Solution Phase. *Langmuir* **2011**, *27*, 104–108.
- Baranov, D.; Manna, L.; Kanaras, A. G. Chemically Induced Self-Assembly of Spherical and Anisotropic Inorganic Nanocrystals. *J. Mater. Chem.* **2011**, *21*, 16694–16703.
- Grzelczak, M.; Vermant, J.; Furst, E. M.; Liz-Marzan, L. M. Directed Self-Assembly of Nanoparticles. *ACS Nano* **2010**, *4*, 3591–3605.
- Li, F.; Josephson, D. P.; Stein, A. Colloidal Assembly: The Road from Particles to Colloidal Molecules and Crystals. *Angew. Chem., Int. Ed.* **2011**, *50*, 360–388.
- Alivisatos, A. P.; Johnsson, K. P.; Peng, X.; Wilson, T. E.; Loweth, C. J.; Bruchez, M. P.; Schultz, P. G. Organization of ‘Nanocrystal Molecules’ Using DNA. *Nature* **1996**, *382*, 609–611.
- Mirkin, C. A.; Letsinger, R. L.; Mucic, R. C.; Storhoff, J. J. A DNA-Based Method for Rationally Assembling Nanoparticles into Macroscopic Materials. *Nature* **1996**, *382*, 607–609.
- Cheng, W. L.; Tan, S. J.; Campolongo, M. J.; Hartman, M. R.; Kahn, J. S.; Luo, D. Bio-mediated Assembly of Ordered Nanoparticle Superstructures. In *Comprehensive Nanoscience and Technology*; Andrews, D. L., Scholes, G. D., Wiederrecht, G. P., Eds.; Academic Press: Amsterdam, The Netherlands, 2010; pp 69–103.
- Knorowski, C.; Travesset, A. Materials Design By DNA Programmed Self-Assembly. *Curr. Opin. Solid State Mater. Sci.* **2011**, *15*, 262–270.
- Macfarlane, R. J.; Lee, B.; Jones, M. R.; Harris, N.; Schatz, G. C.; Mirkin, C. A. Nanoparticle Superlattice Engineering with DNA. *Science* **2011**, *334*, 204–208.
- Nelson, D. R. Toward a Tetravalent Chemistry of Colloids. *Nano Lett.* **2002**, *2*, 1125–1129.
- Zeng, X.; Liu, F.; Fowler, A. G.; Ungar, G.; Cseh, L.; Mehl, G. H.; Macdonald, J. E. 3D Ordered Gold Strings by Coating Nanoparticles with Mesogens. *Adv. Mater.* **2009**, *21*, 1746–1750.
- Motte, L.; Pilieni, M. P. Self-Assemblies of Silver Sulfide Nanocrystals: Influence of Length of Thio-Alkyl Chains Used as Coating Agent. *Appl. Surf. Sci.* **2000**, *164*, 60–67.
- Kahn, M. L.; Monge, M.; Snoeck, E.; Maisonnat, A.; Chaudret, B. Spontaneous Formation of Ordered 2D and 3D Superlattices of ZnO Nanocrystals. *Small* **2005**, *1*, 221–224.
- Rycenga, M.; McLellan, J. M.; Xia, Y. Controlling the Assembly of Silver Nanocubes through Selective Functionalization of Their Faces. *Adv. Mater.* **2008**, *20*, 2416–2420.
- Han, W.; Yi, L.; Zhao, N.; Tang, A.; Gao, M.; Tang, Z. Synthesis and Shape-Tailoring of Copper Sulfide/Indium Sulfide-Based Nanocrystals. *J. Am. Chem. Soc.* **2008**, *130*, 13152–13161.
- Macdonald, J. E.; Bar Sadan, M.; Houben, L.; Popov, I.; Banin, U. Hybrid Nanoscale Inorganic Cages. *Nat. Mater.* **2010**, *9*, 810–815.
- Pinna, N.; Niederberger, M. Surfactant-Free Nonaqueous Synthesis of Metal Oxide Nanostructures. *Angew. Chem., Int. Ed.* **2008**, *47*, 5292–5304.
- Garnweithner, G.; Goldenberg, L. M.; Sakhno, O. V.; Antonietti, M.; Niederberger, M.; Stumpe, J. Large-Scale Synthesis of Organophilic Zirconia Nanoparticles and Their Application in Organic–Inorganic Nanocomposites for Efficient Volume Holography. *Small* **2007**, *3*, 1626–1632.
- Clavel, G.; Willinger, M.-G.; Zitoun, D.; Pinna, N. Manganese-Doped Zirconia Nanocrystals. *Eur. J. Inorg. Chem.* **2008**, *6*, 863–868.
- Ninjabdar, T.; Garnweithner, G.; Börger, A.; Goldenberg, L. M.; Sakhno, O.; Stumpe, J. Synthesis of Luminescent ZrO₂: Eu Nanoparticles and Their Holographic Sub-micrometer Patterning in Polymer Composites. *Adv. Funct. Mater.* **2009**, *19*, 1819–1825.
- Pucci, A.; Clavel, G.; Willinger, M.-G.; Zitoun, D.; Pinna, N. Transition Metal-Doped ZrO₂ and HfO₂ Nanocrystals. *J. Phys. Chem. C* **2009**, *113*, 12048–12058.
- Joo, J.; Yu, T.; Kim, Y. W.; Park, H. M.; Wu, F.; Zhang, J. Z. Hyeon, Multigram Scale Synthesis and Characterization of Monodisperse Tetragonal Zirconia Nanocrystals. *J. Am. Chem. Soc.* **2003**, *125*, 6553–6557.
- Lopez, E. F.; Escribano, V. S.; Panizza, M.; Carnasciali, M. M.; Busca, G. Vibrational and Electronic Spectroscopic Properties of Zirconia Powders. *J. Mater. Chem.* **2001**, *11*, 1891–1897.
- Pinna, N.; Garnweithner, G.; Beato, P.; Niederberger, M.; Antonietti, M. Synthesis of Yttria-Based Crystalline and Lamellar Nanostructures and Their Formation Mechanism. *Small* **2005**, *1*, 112–121.
- Karmaoui, M.; Sa Ferreira, R. A.; Mane, A. T.; Carlos, L. D.; Pinna, N. Lanthanide-Based Lamellar Nanohybrids: Synthesis, Structural Characterization, and Optical Properties. *Chem. Mater.* **2006**, *18*, 4493–4499.
- Karmaoui, M.; Sá Ferreira, R. A.; Mane, A. T.; Carlos, L. D.; Pinna, N. Lanthanide-Based Lamellar Nanohybrids: The Case of Erbium. *Mater. Sci. Eng., C* **2007**, *27*, 1368–1371.
- Ye, X.; Jin, L.; Caglayan, H.; Chen, J.; Xing, G.; Zheng, C.; Doan-Nguyen, V.; Kang, Y.; Engheta, N.; Kagan, C. R.; et al. Improved Size-Tunable Synthesis of Monodisperse Gold Nanorods through the Use of Aromatic Additives. *ACS Nano* **2012**, *6*, 2804–2817.
- Pinna, N. The “Benzyl Alcohol Route”: An Elegant Approach Towards Organic–Inorganic Hybrid Nanomaterials. *J. Mater. Chem.* **2007**, *1*, 2769–2774.
- Mang, X.; Zeng, X. B.; Tang, B.; Liu, F.; Ungar, G.; Zhang, R.; Cseh, L.; Mehl, G. H. Control of Anisotropic Self-Assembly of Gold Nanoparticles Coated with Mesogens. *J. Mater. Chem.* **2012**, DOI: 10.1039/C2JM16794H.